Journal of Alloys and Compounds 509 (2011) 3995–4001

Contents lists available at ScienceDirect

Journal of Alloys and Compounds

journal homepage: www.elsevier.com/locate/jallcom

Effects of Mo additive on the structure and electrochemical properties of low-temperature AB_5 metal hydride alloys

K. Young*, T. Ouchi, B. Reichman, J. Koch, M.A. Fetcenko

Energy Conversion Devices Inc./Ovonic Battery Company, 2983 Waterview Drive, Rochester Hills, MI 48309, USA

ARTICLE INFO

Article history:
Received 1 December 2010
Received in revised form
27 December 2010
Accepted 29 December 2010
Available online 4 January 2011

Keywords:
Hydrogen absorbing materials
Transition metal alloys
Metal hydride electrode
Electrochemical reactions

ABSTRACT

After an annealing treatment at 960 °C for 8 h, the molybdenum added into previously designed AB_5 alloys for −30 °C applications segregates into spheres with diameters between 1 and 10 μm. A secondary phase with Zr-to-other elements ratio of about 1-to-5, over- (AB_7), and under-stoichiometric (AB_4) phases were observed in most of the alloys regardless of Mo-content. As the Mo-content increases, the AB_7 phase disappears while the AB_4 phase grows in size and abundance. Regarding the gaseous absorption properties, a small amount of Mo (0.2 at.%) in the main phase reduces the plateau pressure and hydride heat of formation uniformly for all Mo-containing alloys. The reduction in main phase abundance causes a decrease in both the total and the reversible hydrogen storage capacities. In electrochemical testing, the addition of Mo decreases the discharge capacity, high-rate dischargeability, and hydrogen diffusion in the bulk. The influence of Mo-addition to general battery performance is very minor. However, the low-temperature AC impedance measured at −40 °C shows reduced charge transfer resistance and increased double layer capacitance in the Mo-containing alloys. Mo was found to assist the surface reaction at very low temperatures, and the effect is proportional to the amount of addition as noted by the increasing surface area and catalytic ability, which is similar to the case of AB_2 alloys.

1. Introduction

Recently, AB_2 [1–8], AB_3 [9–11], and AB_5 [12–15], and BCC [16,17] metal hydride (MH) alloys have been intensively investigated to improve the performance of nickel metal hydride (Ni/MH) batteries. In one direction of compositional modification, molybdenum was found to be beneficial to the low-temperature applications of Ni/MH batteries [18–21]. In the AB_2 alloy system, we previously reported the positive contribution of Mo to low-temperature performance through the increase in bulk diffusion rate, surface area, and surface catalytic ability [21]. In an AB_5 system, Senoh et al. found that the addition of Mo in an AB_5 alloy improved the −40 °C charge efficiency through the enhancement of surface charge-transfer reaction [20]. The improvement in low-temperature performance in the Mo-containing AB_5 alloy was later confirmed by Iwakura et al. and connected to its better bulk hydrogen diffusion and surface charge-transfer reaction [22]. As for the other properties of Mo-modified AB_5 alloys, Osumi et al. reported an increase in pressure–concentration–temperature (PCT) isotherm hysteresis in the $MmNi_{4.7}Al_{0.3}Mo_{0.1}$ alloy [23]. Notten and Hokkeling found that a $MoCo_3$ catalytic secondary phase was formed in the Mo-doped over-stoichiometric $AB_{5.5}$ alloy with quick quench on a chilled plate [18] or the melt-spun alloy with a follow-up annealing at 900 °C [24]. Jakšić demonstrated a dramatic reduction in overpotential in the alloy that had its surface modified by galvanic codeposition of Mo and Co [25]. The $MoCo_3$ phase was confirmed by Hsu et al. with selective area diffraction pattern using transmission electron microscopy [26]. The same group also reported an increased hydrogen storage capacity with the substitution of Ni or Co by Mo [27,28]. Small amounts of Mo-substitution were found by Ye and Zhang to increase the room temperature high-rate dischargeability (HRD) and surface charge-transfer current [29,30]. Although the general characteristics of Mo-modified AB_5 alloys have been reported, a more systematic study on the influences of Mo to the structural, gaseous storage, and electrochemical properties (especially at low temperature) is needed and will be presented in this paper.

2. Experimental setup

In this study, induction melting was performed under an argon atmosphere in a 2 kg furnace using a $MgAl_2O_4$ crucible, an alumina tundish, and a steel pancake-shape mold. The ingots were annealed in vacuum (1×10^{-8} torr) at 960 °C for 8 h before being mechanically crushed into −200 mesh powder. The chemical composition of each sample was examined by a Varian *Liberty* 100 inductively coupled plasma (ICP) system. A Philips *X'Pert Pro* X-ray diffractometer (XRD) was used to study the microstructure, and a JOEL-*JSM6320F* scanning electron microscope (SEM) with energy dispersive spectroscopy (EDS) capability was used to study the phase distribution and composition. PCT characteristics for each sample were measured

* Corresponding author. Tel.: +1 248 293 7000; fax: +1 248 299 4520.
E-mail address: kwoyoung@yahoo.com (K. Young).

0925-8388/$ – see front matter © 2011 Elsevier B.V. All rights reserved.
doi:10.1016/j.jallcom.2010.12.205

Table 1
Design composition and ICP result.

		La at.%	Ce at.%	Pr at.%	Nd at.%	Ni at.%	Co at.%	Mn at.%	Al at.%	Cu at.%	Zr at.%	Mo at.%
Mo0	Design	10.5	4.3	0.5	1.4	64.3	5.0	4.6	6.0	3.2	0.2	0.0
	ICP	9.9	4.3	0.4	1.3	65.4	5.1	4.6	5.5	3.3	0.2	0.0
Mo1	Design	10.5	4.3	0.5	1.4	63.3	5.0	4.6	6.0	3.2	0.2	1.0
	ICP	10.1	4.2	0.4	1.2	64.2	5.1	4.5	5.6	3.2	0.2	1.3
Mo2	Design	10.5	4.3	0.5	1.4	62.3	5.0	4.6	6.0	3.2	0.2	2.0
	ICP	9.9	4.5	0.5	1.3	63.4	5.0	4.4	5.6	3.2	0.2	2.0
Mo3	Design	10.5	4.3	0.5	1.4	61.3	5.0	4.6	6.0	3.2	0.2	3.0
	ICP	9.9	4.5	0.5	1.2	61.8	5.2	4.6	5.8	3.2	0.2	3.1
Mo4	Design	10.5	4.3	0.5	1.4	60.3	5.0	4.6	6.0	3.2	0.2	4.0
	ICP	10.1	4.4	0.4	1.2	61.0	5.0	4.6	5.9	3.3	0.2	3.8

using a Suzuki-Shokan multi-channel PCT system. In the PCT analysis, each sample was first activated by a 2-h thermal cycle between 300 °C and room temperature at 25 atm H_2 pressure; then, PCT isotherms at 30 °C and 60 °C were measured. Details of both electrode and cell preparations as well as measurement methods have been reported before [31,32]. The hydrogen diffusion and surface charge-transfer current measurements were performed in Arbin Instruments BT4+ Portable Battery Test System. AC impedance measurements were conducted using Solartron 1250 Frequency Response Analyzer with sine wave of amplitude 10 mV and frequency range of 10 mHz to 10 kHz. Prior to the measurements, the electrodes were subjected to one full charge/discharge cycle at *C*/10 rate using a Solartron 1470 Cell Test galvanostat, then recharged to 100% state-of-charge (SOC), subsequently discharged to 80% (SOC), and finally cooled to −40 °C.

3. Results and discussion

Five alloys with Mo substituting for Ni at various concentration levels from 0 to 4 at.% were prepared, and the design compositions are listed in Table 1. The base alloy (Mo0) with no Mo substitution was selected from an earlier study for its good low-temperature performance at −30 °C [33]. The base alloy is a derivative of La-rich misch metal based AB_5 alloy. Cu was added to engineer the shape of metallic inclusions and to create tunnels in the surface oxide interfaces [34]. Zr was added to increase the cycle life as compensation for the reduced amount of Co used in the alloy [35]. The ICP results of all five alloys, as listed in Table 1, are very close to the design compositions. Small amounts of La and Al went into the slag and were removed by the tundish.

3.1. XRD structure analysis

The XRD spectra of the five alloys before and after annealing are shown in Figs. 1 and 2, respectively. The base alloy Mo0 shows a typical $CaCu_5$ structure before and after annealing. From the spectra of alloys before annealing, Mo peaks only become visible with the highest Mo-content (Mo4). After annealing, the diffraction peaks from Mo phase start to grow as early as Mo1. At the higher Mo-content levels (Mo3 and Mo4), the peaks from the $MoNi_4$ phase start to appear. Other minor phases are not recognizable in the XRD analysis due to their low percentages. Each sample's lattice constants *a* and *c* from the $CaCu_5$ structure were calculated and are listed in Table 2. Lattice constant *a* of each alloy with Mo is similar

Table 2
Lattice constants *a* and *c*, *c*/*a* ratio, $CaCu_5$ lattice volume, full width at half maximum (2θ, in degrees) for (0 0 1) reflection peak, and corresponding crystallite size from XRD analysis.

Alloy #	*a* (Å)	*c* (Å)	*c*/*a*	V_{CaCu_5} (Å^3)	FWHM (0 0 1)	Crystallite size (Å)
Mo0	5.011	4.048	0.8078	88.03	0.169	826
Mo1	5.021	4.050	0.8066	88.42	0.183	704
Mo2	5.021	4.051	0.8068	88.45	0.166	859
Mo3	5.018	4.048	0.8067	88.27	0.201	601
Mo4	5.019	4.051	0.8071	88.37	0.144	>1000

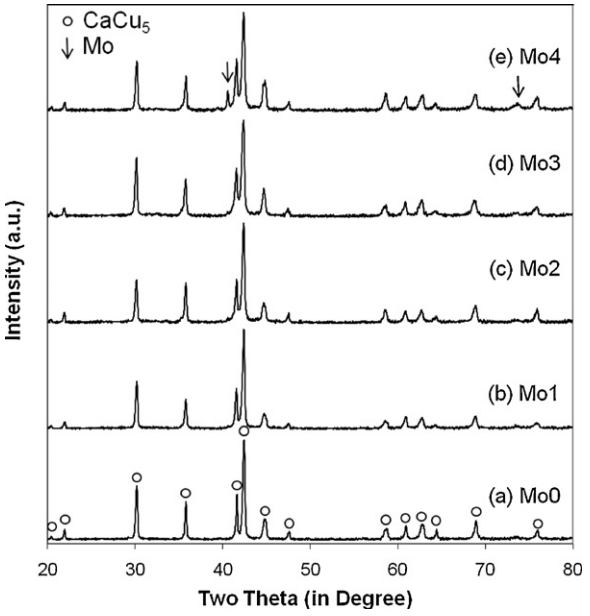

Fig. 1. XRD spectra using Cu-K_α as the radiation source for alloys Mo0 (a), Mo1 (b), Mo2 (c), Mo3 (d), and Mo4 (e). Diffraction peaks from Mo are visible only in (e).

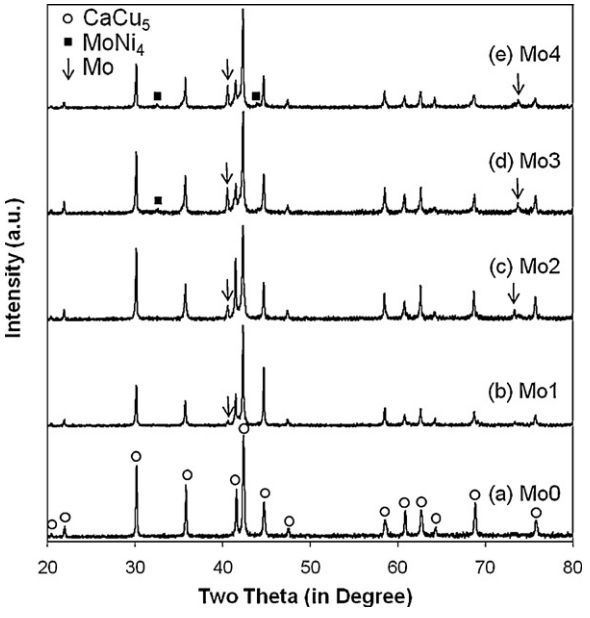

Fig. 2. XRD spectra using Cu-K_α as the radiation source for after annealed alloys Mo0 (a), Mo1 (b), Mo2 (c), Mo3 (d), and Mo4 (e). Diffraction peaks from Mo are recognized with all Mo-contents, and peaks from $MoNi_4$ are visible with higher Mo-contents.

Table 3
EDS result in atomic percentage from area identified in SEM micrograph (Fig. 2).

	La at.%	Ce at.%	Pr at.%	Nd at.%	Ni at.%	Co at.%	Mn at.%	Al at.%	Cu at.%	Zr at.%	Mo at.%	B/A ratio	Phase
Mo0-1	70.5	9.8	0.0	2.7	9.7	0.2	0.0	1.4	1.0	4.6	0.0	0.2	La
Mo0-2	**10.1**	**4.8**	**0.0**	**1.2**	**63.8**	**4.7**	**6.3**	**5.6**	**3.4**	**0.1**	**0.0**	**5.2**	**Main AB_5**
Mo0-3	0.9	0.5	0.0	0.0	39.5	4.1	21.3	14.8	0.8	18.2	0.0	70.5	$ZrNi_5$
Mo1-1	3.9	2.2	0.0	0.2	33.1	2.8	2.5	2.7	1.7	1.2	49.7	14.9	Mo
Mo1-2	10.7	5.9	0.0	0.5	68.2	4.8	4.4	2.2	2.9	0.1	0.2	4.8	AB_5
Mo1-3	10.0	4.7	0.0	0.3	68.2	4.9	4.2	4.3	3.1	0.1	0.2	5.7	AB_5
Mo1-4	**10.7**	**4.6**	**0.0**	**0.4**	**67.1**	**4.8**	**4.2**	**4.8**	**3.1**	**0.1**	**0.2**	**5.4**	**Main AB_5**
Mo1-5	8.1	4.3	0.0	0.3	68.3	4.8	4.5	6.1	3.1	0.2	0.3	6.9	AB_7
Mo1-6	8.1	4.4	0.0	0.4	70.4	5.1	3.8	4.7	2.9	0.1	0.1	6.8	AB_7
Mo1-7	2.9	1.4	0.0	0.1	22.7	1.9	1.5	1.7	1.4	65.6	0.8	21.7	ZrO_2
Mo1-8	7.6	4.4	0.0	0.6	66.6	4.6	3.9	9.4	2.7	0.1	0.1	6.9	AB_7
Mo2-1	1.0	0.3	0.0	0.0	1.4	0.4	0.3	1.2	0.3	4.6	90.4	75.8	Mo
Mo2-2	12.0	6.9	0.0	0.7	65.2	4.7	4.5	2.7	2.7	0.3	0.2	4.1	AB_4
Mo2-3	13.6	5.4	0.0	0.6	63.8	4.3	4.5	4.1	3.2	0.2	0.2	4.1	AB_4
Mo2-4	**9.9**	**4.7**	**0.0**	**0.5**	**64.9**	**4.4**	**6.1**	**5.6**	**3.5**	**0.1**	**0.2**	**5.6**	**Main AB_5**
Mo2-5	0.4	1.8	0.0	0.0	58.2	10.3	10.4	1.5	1.3	15.7	0.2	44.3	$ZrNi_5$
Mo3-1	1.2	0.3	0.0	0.0	1.3	0.3	0.3	0.7	0.3	5.2	90.4	65.7	Mo
Mo3-2	12.1	6.8	0.0	0.8	64.6	5.0	4.2	2.8	3.0	0.3	0.3	4.1	AB_4
Mo3-3	**10.2**	**4.5**	**0.0**	**0.7**	**64.8**	**5.2**	**4.6**	**6.5**	**3.3**	**0.1**	**0.2**	**5.5**	**Main AB_5**
Mo3-4	0.3	1.4	0.0	0.0	57.4	10.1	11.7	2.2	1.1	15.3	0.4	57.8	$ZrNi_5$
Mo4-1	46.3	3.1	0.0	0.0	45.7	0.2	0.0	0.0	4.5	0.0	0.2	1.0	La
Mo4-2	1.4	0.3	0.0	0.0	1.3	0.4	0.2	0.8	0.4	5	90.2	57.8	Mo
Mo4-3	13.0	6.7	0.0	0.7	63.5	4.5	5.1	3.5	2.7	0.3	0.1	3.9	AB_4
Mo4-4	**10.6**	**4.7**	**0.0**	**0.7**	**64.6**	**5.0**	**4.1**	**6.7**	**3.2**	**0.1**	**0.2**	**5.2**	**Main AB_5**
Mo4-5	0.1	1.1	0.0	0.0	56.7	10.2	12.6	2.5	0.6	15.8	0.4	82.3	$ZrNi_5$

or larger than that of Mo0 while lattice constant *c* is about the same. The *c*/*a* aspect ratio decreases with the addition of Mo in the alloy and predicts a negative influence on the cycle life performance [23]. The $CaCu_5$ unit cell volumes calculated from the lattice constants are similar among the alloys with Mo addition and larger than that of the base alloy Mo0. The increase in unit cell volume implies the Mo-containing alloys have stronger metal-hydrogen bond strength and consequently lower equilibrium plateau pressure. The crystallite sizes estimated from the full-width at half maximum (FWHM) of the $CaCu_5$ (0 0 1) diffraction peak are also listed in Table 2. The general tendency of the crystallite size on Mo-content is difficult to establish and related to the multi-phase nature of the alloys as shown in the next section.

3.2. SEM/EDS phase analysis

The microstructures for this series of alloys were studied by SEM. Back-scattering electron images (BEI) are presented in Fig. 3. The compositions in several areas identified numerically in the micrographs were studied by EDS and the results are listed in Table 3. In the Mo-free base alloy (Mo0, Fig. 3a), the main AB_5 phase with composition close to the design value appears to be very uniform with occasional La–Ce metal inclusions and a secondary phase with lower atomic mass (darker in BEI micrograph). This secondary phase is mainly Ni, Mn, Zr, and Al and assigned as $ZrNi_5$ based on the composition. The amount of the secondary phase is too small to be recognized by XRD analysis. The $ZrNi_5$ phase is also a hydrogen storage alloy, especially when a part of Ni is replaced by Co [36,37]. The solubility of Al in this alloy is also large according to a previous study [38]. The La–Ce inclusion contains a much higher level of Zr compared to the main working phase.

After annealing, Mo segregates out and forms spheres with diameters between 1 and 10 μm. As the Mo-content in the alloy increases, the volume percentage of the Mo inclusions also increases. The Mo inclusions deprive the main AB_5 phase of Zr, similar to what the La–Ce phase does in Mo0. Due to the limitation in SEM resolution, individual $MoNi_4$ phases were not found and may reside between the Mo and AB_5 phases. The composition of the main phases (in bold in Table 3) in the alloys is similar to the design values. The stoichiometry (B/A ratio) of the main phase for each alloy is above 5.0; however, it increases from 5.2 (Mo0) to 5.6 (Mo2) and then decreases to 5.2 (Mo4). The Cu content in the main phase of each alloy is very close to the design composition. The amount of Zr in the main phase is only half of the design as the rest goes into the other secondary phases. After the formation of Mo inclusions, the Mo content in the main phase of each Mo-containing alloy is small and similar (0.2 at.%) due to the limited solubility of Mo in $LaNi_5$. In addition to the main phase, other secondary phases with stoichiometries close to AB_5 are also found and the total abundance of these phases increases with the increase in Mo-content. In Mo1 (Fig. 3b), only very small amounts of AB_5 with slightly higher Ni-content and AB_7 phases are found. The AB_7 phase should be considered as an over-stoichiometric AB_5 phase with excess B atoms since the La–Ni binary phase diagram does not offer such intermetallic compound. In the next alloy of this sequence (Mo1), a larger size of the AB_4 phase (an under-stoichiometric AB_5 phase) was found (Fig. 3c). This AB_4 phase, also considered to have a $CaCu_5$ structure as in AB_7 phase, continues to grow in size with further increases in Mo-content (Mo3 and Mo4) (Fig. 3d and e). The size of the $ZrNi_5$ phase, similar to the AB_4 phase, increases as the Mo-content raises, and the $ZrNi_5$ phase is always enclosed by the AB_4 phase. The abundance of phases cannot be estimated from the SEM micrographs. These micrographs are not typical representations of the average phase structure. Regions with the largest amount of secondary phases were chosen to better illustrate their sizes and shapes.

3.3. Gaseous study

Gaseous hydrogen storage properties of the alloys were studied by PCT. The resulting absorption and desorption isotherms measured at 30 °C and 45 °C for alloys Mo0 and Mo1 are shown in Fig. 4a and b, respectively. The information obtained from the PCT study is summarized in Table 4. The plateau pressures are similar among the Mo-doped alloys and lower than that of Mo-free Mo0 alloy. According to the EDS analysis on the main phases (phases in bold in Table 3), the Mo contents of all Mo-doped alloys are the same (0.2 at.%), and the extra Mo segregates into the secondary phases. Therefore, the enlargement of the $CaCu_5$ unit cell due to the addition of Mo is similar for each Mo-containing alloy, and,

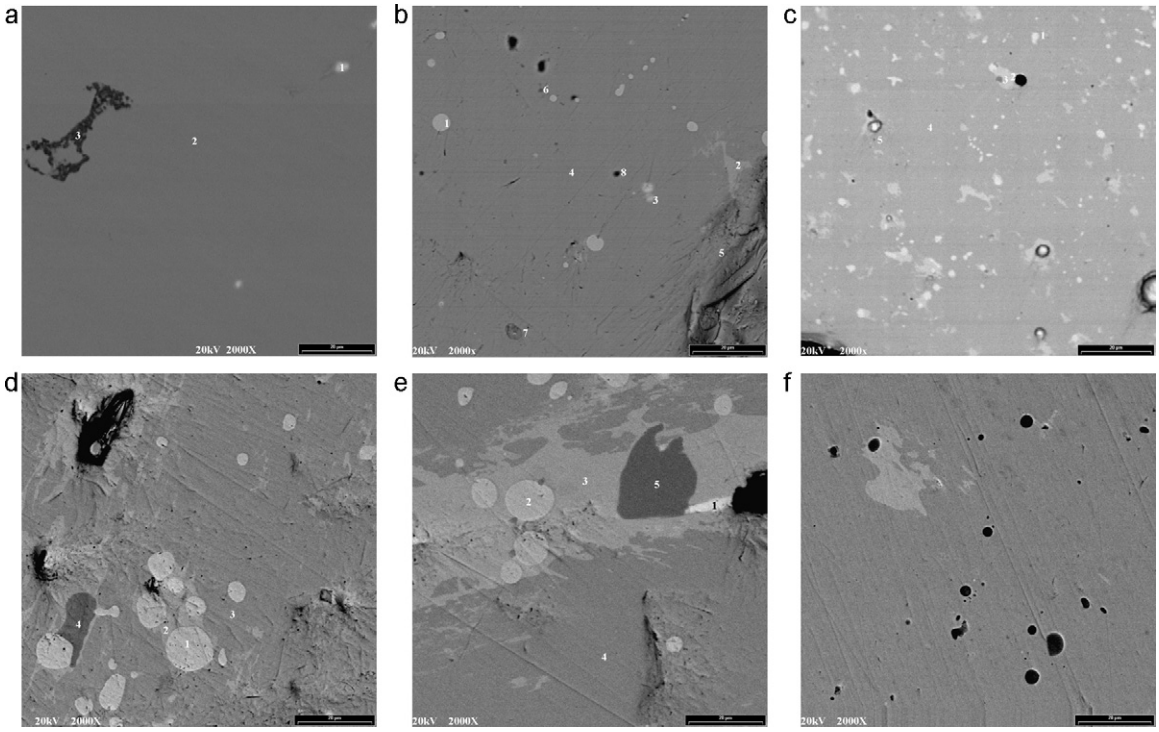

Fig. 3. SEM backscattering images for after annealed alloys Mo0 (a), Mo1 (b), Mo2 (c), Mo3 (d), Mo4 (e), and Mo1 after etching in 100 °C 30% KOH solution for 4 h (f).

consequently, the amount of reduction in plateau pressure is also very similar.

The slope factor (SF) is defined as the ratio of the storage capacity between 0.01 and 0.5 MPa hydrogen pressure to the total capacity. SF of each alloy is listed in Table 4 and can be used to determine the degree of disorder in the alloy [39,40]. As the Mo-content increases, the SF first remains about the same and then decreases. The alloys with the higher Mo-content (Mo3 and Mo4) are less homogeneous according to the SF values. The hysteresis of the PCT isotherm, listed in Table 4, is defined as $\ln(P_a/P_d)$, where P_a and P_d are the absorption and desorption equilibrium pressures at 0.6 wt.%, respectively. The hysteresis can be used to predict the pulverization rate of the alloy during cycling [41]. In this case, the hysteresis first increases and then decreases to the original value as the Mo-content increases. The contents of Cu and Zr in the main phase, which are very important for PCT hysteresis, are very similar for all the alloys and should not be taken into account regarding any changes in the PCT hysteresis. The initial increase in the PCT hysteresis is due to the incorporation of Mo in the main phase, which results in a positive contribution [42]. As the Mo-content further increases, the Al content in the main phase increases. According to the calculations using density of function and full potential linearized augmented waves, Al substitution occupies mainly the 3 g site and causes an increase in c/a aspect ratio [42]. This agrees with the general trend of c/a ratios found in the XRD analysis of Mo-containing alloys. The increased c/a aspect ratio reduces the PCT hysteresis [23].

With increasing Mo-content, both the maximum and reversible hydrogen storage capacities decrease. The addition of Mo in the alloy is supposed to increase the storage capacity; however, the amount of Mo in the main working phase is very small (0.2 at.% according to EDS analysis). With the increase in Mo-content, the percentage of the main phase with the desirable stoichiometry

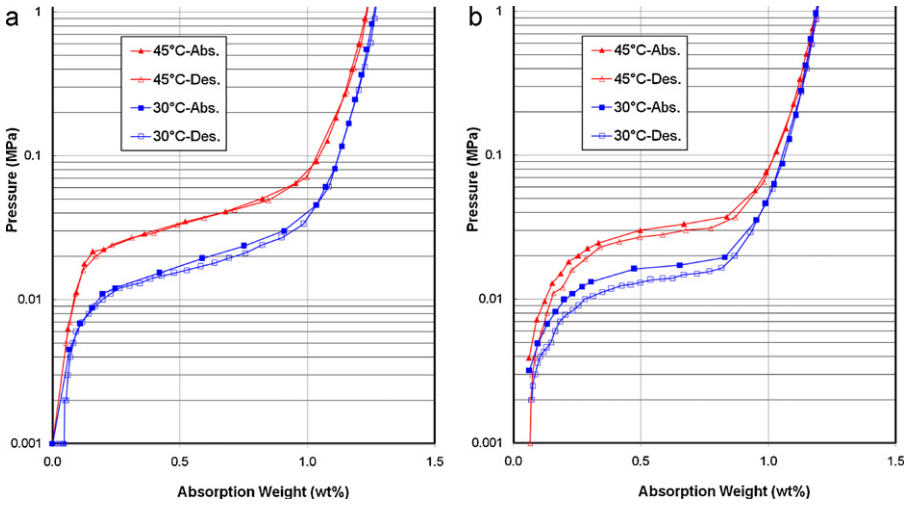

Fig. 4. 30 °C and 45 °C PCT isotherms of alloys Mo0 (a) and Mo1 (b). Solid and open symbols are for absorption and desorption curves, respectively.

Table 4
Summary of gaseous properties (plateau pressure, slope factor, hysteresis, maximum capacity, change in enthalpy, and change in entropy), and results from half-cell measurement (pre-charge, capacities, high-rate dischargeability, diffusion coefficient, and exchange current) and full-cell (cycle life, charge retention, specific power, and low-temperature performance) measurement.

	Des. pressure at 0.6% at 30 °C	Slope factor at 30 °C	PCT hysteresis at 0.6% at 30 °C	Max. cap. at 30 °C	Rev. cap. at 30 °C	$-\Delta H$	$-\Delta S$	Pre-charge	Cap. at 300 mA/g	Cap. at 5 mA/g	HRD	Diffusion coeffi-cient	Exchange current	70% cycle life	30-Day charge retention	Room temp. specific power	Low-temp. at −10 °C 0.5C	Charge transfer resistance at −40 °C	Double-layer capacitance at −40 °C
Unit	MPa	%		wt.%	wt.%	kJ /mole	J/mole K	mAh/g	mAh/g	mAh/g		10^{-10} cm^2/s	mA/g	cycles	%	W/kg	%	Ω g	Farad/g
Mo0	0.018	86	0.13	1.26	1.21	39.9	117	0	318	336	0.946	10.9	33.1	135	76	179	89	5.4	1.02
Mo1	0.013	83	0.24	1.21	1.15	42.8	124	10	258	302	0.854	9.3	25.9	150	71	166	89	3.7	1.42
Mo2	0.011	87	0.25	1.22	1.15	43.8	122	19	267	314	0.850	9.4	32.3	80	73	174	90	4.0	1.32
Mo3	0.013	77	0.13	1.14	1.07	44.7	118	37	255	304	0.839	9.4	30.2	65	68	146	91	3.7	1.23
Mo4	0.012	73	0.15	1.10	1.01	41.7	119	19	234	301	0.777	9.4	36.8	105	72	127	90	4.2	1.13

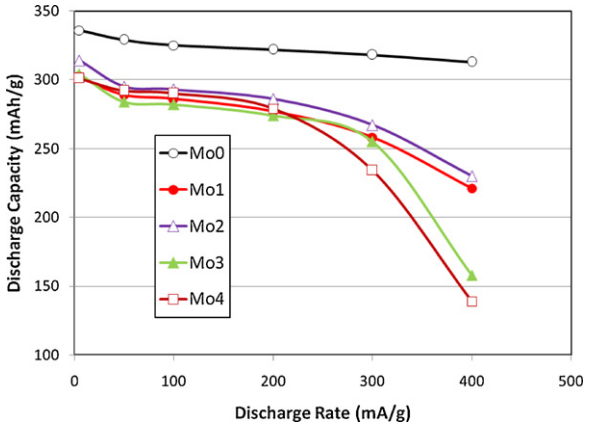

Fig. 5. The rate-dependency of discharge capacity from half-cell measurement for alloys Mo0 to Mo4.

decreases (as seen from the SEM micrographs in Fig. 3), and this consequently deteriorates the storage capacity.

Desorption equilibrium pressures at 0.6 wt. % storage capacity measured at 30 and 45 °C were used to calculate the changes in enthalpy (ΔH) and entropy (ΔS) by the equation

$$\Delta G = \Delta H - T\,\Delta S = RT \ln P \quad (1)$$

where R is the ideal gas constant and T is the absolute temperature. The results of these calculations are listed in Table 4. Hydride heat of formation of the Mo0 alloy is higher than that from $LaNi_5$ due to the additions of Al and Cu [43]. Hydride heats of formation above 40 kJ/mole H_2 can be found in alloys with similar compositions [44]. The value of each Mo-containing alloy is even higher than that of Mo-free Mo0 alloy, which agrees with the plateau pressure results. The ΔS values are very similar and close to the ΔS between the hydrogen gas and hydrogen in the solid [45].

3.4. Electrochemical measurement

Discharge capacities of the five alloys were measured in a flooded cell against a partially pre-charged $Ni(OH)_2$ as the positive electrode. Unlike AB_2 alloys, pre-activation in hot alkaline was not performed. The cell was first discharged with a small current density at 5 mA/g. The initial discharge capacity before any charge input is due to the hydrogen absorption generated as a result of the metal oxidation in the electrolyte, and it can be used to quantify the ease of activation [46]. A higher initial discharge capacity can be correlated to easier oxidation/activation of the alloy. The amount of pre-charge in mAh/g for each alloy is listed in Table 4. Since Mo with the highest leaching rate [47] was not removed by a pre-activation process, a large amount of pre-charge was found in each Mo-containing alloy due to the oxidation of Mo in KOH electrolyte, which is different from the case of in AB_2 [21].

Discharge capacities of the first cycle at different discharge rates after are plotted in Fig. 5. The discharge capacities at 300 and 5 mA/g are listed in Table 4. The discharge capacities of the Mo-containing alloys are lower than that of the Mo-free alloy for the same reason as why the Mo-containing alloys have lower gaseous hydrogen storage capacities as found from the PCT analysis. The half-cell HRD of each alloy, defined as the ratio of discharge capacity measured at 300 mA/g to that at 5 mA/g, is listed in Table 4 and plotted in Fig. 6. The half-cell HRD values of Mo-containing alloys are lower than that from the Mo-free alloy. Mo4, with the highest Mo-content, shows the lowest HRD value. The Mo-inclusion and other secondary phases may cause the reduction in discharging at high rate.

Both the bulk diffusion coefficient (D) and the surface exchange current (I_o) are important parameters for analyzing the MH alloy

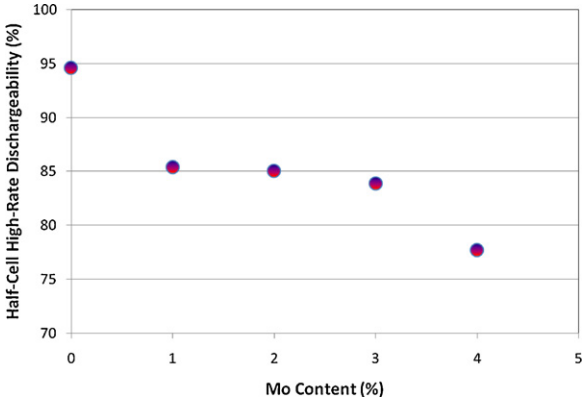

Fig. 6. The half-cell HRD as defined by the ratio of capacity at 300 mA/g discharge current to that at 5 mA/g vs. the Mo-content in the alloy.

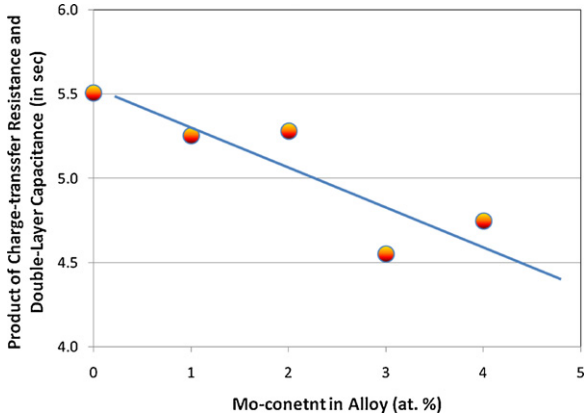

Fig. 7. The product of charge-transfer resistance and double-layer capacitance measured at −40 °C as a function of Mo-content in the alloy.

for use in sealed Ni/MH battery. The details of both measurements were previously reported [48], and the values are listed in Table 4. The D values for all Mo-containing alloys are similar and lower than that of the Mo-free alloy. The Mo-inclusion and Mo-induced secondary phases contribute negatively to the diffusion of hydrogen in the bulk. The results of I_o measurement are less conclusive. The I_o values vary in a range and no specific trend can be found with respect to the Mo-content.

Four important Ni/MH technical parameters (cycle life, charge retention, specific power, and low-temperature performance) for the MH electrode made from each alloy are listed in Table 4. The cycle life performance (measured by the number of cycles reaching 70% of the original capacity) does not show clear correlation to the PCT hysteresis and therefore is not dominated by pulverization. The complicated nature of the multi-component feature in the alloy bulk, as shown in the SEM micrographs, makes the search for the reason of cycle life fluctuation very difficult.

The 30-day charge retention values are listed in Table 4. Charge retentions of the Mo-containing alloys are slightly worse than that of the Mo-free base alloy. The more corrosion-resistant nature found in Mo-containing AB_2 surface [21] was not observed here. The room temperature specific power densities measured at 80% SOC are listed in Table 4. The specific power matches the trend of half-cell HRD. This agreement between half-cell and sealed-cell high-rate performance is true for Mo-containing AB_5 alloys, but not for AB_2 alloys, which deserves further investigation.

Low-temperature performance, defined as the ratio of the capacity measured at 0.5C rate and −10 °C to the capacity measured at the same rate and room temperature, is listed in Table 4 for each of the alloys. All alloys in this study show similar results. The −10 °C performance is dominated by the shape of the metallic inclusions and the tunnels in the surface oxide engineered by the Cu-addition. The designed Cu-contents of all alloys are the same; moreover, the EDS analysis shows the same percentage in the main $CaCu_5$ working phase which guarantees good −10 °C performance.

The low-temperature characteristic of these alloys was further studied by taking AC impedance measurements conducted at −40 °C. The charge-transfer resistance (R) and double-layer capacitance (C) were calculated from the Cole–Cole plot and are listed in Table 4. All the Mo-containing alloys show lower R values than the Mo-free Mo0 alloy. The C values indicate the larger surface areas of the Mo-containing alloys. The increase in the surface area of the Mo-containing alloys is the result of the high solubility of Mo in the alkaline solution as can found in the Pourbaix Diagram [49]. Similar phenomenon was reported by Au et al. [47]. Removing Mo-inclusions from the surface increases the surface roughness and thus contributes to a 15–40% increase in surface area. To illustrate the scenario, an SEM micrograph from Mo1 surface after etching in 100 °C 30% KOH solution for 4 h is shown in Fig. 3f. The dark circles in the graph are the etching pits from the Mo-inclusions. In general, the product of R and C, as plotted in Fig. 7, drops as the Mo-content increases. Therefore, Mo addition is considered to contribute positively to the surface catalytic reaction. The general trend of the product of R and C at −40 °C is very similar to that in the cases of AB_2 (Fig. 6 in Ref. [4]). However, the AB_5 alloys have about one order of magnitude lower R and one order of magnitude larger C when compared to those of the AB_2 alloys. Therefore, according to current study, AB_5 alloys are more suitable for −40 °C low temperature applications. In conclusion, similar to Mo addition in AB_2 alloys [21], the improvement in low-temperature performance by Mo-addition to AB_5 alloy is through a combination of increasing the surface area and the surface catalytic ability. When comparing the charge transfer resistance measured at −40 °C to the exchange current measured at room temperature, we see that while all Mo-containing alloys show lower resistance at −40 °C, the Mo1, Mo2, and Mo3 alloys show lower exchange current at room temperature. This discrepancy suggests that the surface area plays an important role at −40 °C and that other factors, such as metal-hydrogen bond strength (as seen from ΔH values), may have a stronger influence at room temperature.

4. Summary and conclusions

The Mo addition to an AB_5 alloy previously designed for −30 °C low-temperature performance shows an improvement in the −40 °C half-cell measurement. Similar to AB_2 alloys, the improvement at −40 °C is achieved through the combination of increasing both surface catalytic ability and surface area. The later was accomplished by the preferential etching of Mo-inclusions formed through the annealing process. In the phase analysis, in addition to spherical Mo-inclusions, inclusions with high Zr-content (mainly $ZrNi_5$ with occasionally ZrO_2), over-stoichiometric phases (with composition close to AB_7), and under-stoichiometric phases (close to AB_4) are also found. The sizes of the secondary phases increase as the Mo-content increases. Since most of the Mo and Zr move to the secondary phases after annealing, the chemical compositions of the main AB_5 phases in all Mo-containing alloys are similar. The addition of Mo at levels between 1 and 4 at.% increases the lattice constant a, the $CaCu_5$ unit cell volume, and the absolute value of the hydride heat of formation, lowers the gaseous equilibrium pressure, decreases both the maximum and reversible hydrogen storage capacity, and reduces the electrochemical discharge capacity, HRD, bulk hydrogen diffusion, and room temperature specific power.

References

[1] K. Young, M.A. Fetcenko, F. Li, T. Ouchi, J. Koch, J. Alloys Compd. 468 (2009) 482.
[2] K. Young, M.A. Fetcenko, T. Ouchi, F. Li, J. Koch, J. Alloys Compd. 469 (2009) 406.
[3] I. Saldan, J. Frenzel, O. Shekhah, R. Chelmowski, A. Birkner, Ch. Wöll, J. Alloys Compd. 470 (2009) 568.
[4] S. Qiu, H. Chu, Y. Zhang, D. Sun, X. Song, L. Sun, F. Xu, J. Alloys Compd. 471 (2009) 453.
[5] K. Young, T. Ouchi, B. Reichman, W. Mays, R. Regmi, G. Lawes, M.A. Fetcenko, A. Wu, J. Alloys Compd. 489 (2010) 202.
[6] K. Young, T. Ouchi, B. Huang, B. Chao, M.A. Fetcenko, L.A. Bendersky, K. Wang, C. Chiu, J. Alloys Compd. 506 (2010) 841.
[7] K. Young, J. Nei, T. Ouchi, M.A. Fetcenko, J. Alloys Compd. (2010), doi:10.1016/j.jallcom.2010.11.005.
[8] A. Guéguen, J.-M. Joubert, M. Latroche, J. Alloys Compd. (2010), doi:10.1016/j.jallcom.2010.10.213.
[9] Y. Chai, K. Asano, K. Sakaki, H. Enoki, E. Akiba, J. Alloys Compd. 485 (2009) 174.
[10] Y. Zhao, M. Gao, Y. Liu, L. Huang, H. Pan, J. Alloys Compd. 496 (2010) 454.
[11] Y. Liu, Y. Cao, L. Huang, M. Gao, H. Pan, J. Alloys Compd. 509 (2011) 675.
[12] E.A. Kumar, M.P. Maiya, S.S. Murthy, B. Viswanathan, J. Alloys Compd. 476 (2009) 92.
[13] Z. Zhou, Y. Song, S. Cui, C. Huang, W. Qian, C. Lin, Y. Zhang, Y. Lin, J. Alloys Compd. 501 (2010) 47.
[14] X.H. An, Y.B. Pan, Q. Luo, X. Zhang, Y.Z. Zhang, Q. Li, J. Alloys Compd. 506 (2010) 63.
[15] M. Tliha, S. Boussami, H. Mathlouthi, J. Lamloumi, A. Percheron-Guégan, J. Alloys Compd. 506 (2010) 559.
[16] M. Gao, S. Zhang, H. Miao, Y. Liu, H. Pan, J. Alloys Compd. 489 (2010) 552.
[17] H. Miao, W. Wang, J. Alloys Compd. 508 (2010) 592.
[18] P.H.L. Notten, P. Hokkeling, J. Electrochem. Soc. 138 (1991) 1877.
[19] Y. Tsuji, O. Yamamoto, Y. Yamamura, H. Seri, Y. Toyoguchi, US Patent 5,753,054 (1998).
[20] H. Senoh, Y. Hara, H. Inoue, C. Iwakura, Electrochim. Acta 46 (2001) 967.
[21] K. Young, T. Ouchi, B. Huang, B. Reichman, M.A. Fetcenko, J. Alloys Compd. (10-03478), submitted for publication.
[22] C. Iwakura, H. Senoh, K. Morimoto, Y. Hara, H. Inoue, Electrochemistry 70 (2002) 2.
[23] Y. Osumi, H. Suzuki, A. Kato, K. Oguro, S. Kawai, M. Kaneko, J. Less-Comm. Met. 89 (1983) 287.
[24] P.H.L. Notten, J.L.C. Daams, R.E.F. Einerhand, Ber. Bunsenges. Phys. Chem. 96 (1992) 656.
[25] M.M. Jakšić, Int. J. Hydrogen Energy 11 (1986) 519.
[26] S.E. Hsu, M.T. Yeh, I.C. Hsu, J.Y. Wang, V. Beibutian, J. Alloys Compd. 293–295 (1999) 658.
[27] M.T. Yeh, V.M. Beibutian, S.E. Hsu, J. Alloys Compd. 293–295 (1999) 721.
[28] S.E. Hsu, V.M. Beibutian, M.T. Yeh, J. Alloys Compd. 330–332 (2002) 882.
[29] H. Ye, H. Zhang, Adv. Eng. Mater. 3 (2001) 481.
[30] H. Ye, H. Zhang, J. Grad. Sch. Chin. Acad. Sci. 20 (2003) 381.
[31] K. Young, M.A. Fetcenko, T. Ouchi, F. Li, J. Koch, J. Alloys Compd. 464 (2008) 238.
[32] K. Young, M.A. Fetcenko, J. Koch, K. Morii, T. Shimizu, J. Alloys Compd. 486 (2009) 559.
[33] K. Young, T. Ouchi, M.A. Fetcenko, U.S. Patent 7,344,677 B2 (2008).
[34] M.A. Fetcenko, S.R. Ovshinsky, K. Young, B. Reichman, T. Ouchi, J. Koch, W. Mays, U.S. Patent 6,830,725 (2004).
[35] M.A. Fetcenko, K. Young, S.R. Ovshinsky, T. Ouchi, U.S. Patent 7,393,500 B2 (2008).
[36] K. Giza, H. Bala, V.V. Pavlyuk, Corros. Sci. 45 (2003) 2055.
[37] K. Giza, H. Bala, Mater. Chem. Phys. 83 (2004) 120.
[38] K. Giza, H. Bala, E. Owczarek, V.V. Pavlyuk, Phys.-Chem. Mech. Mater. 5 (special issue) (2006) 236.
[39] K. Young, T. Ouchi, J. Koch, M.A. Fetcenko, J. Alloys Compd. 477 (2009) 749.
[40] K. Young, T. Ouchi, M.A. Fetcenko, R.K. Regmi, G. Lawes, J. Alloys Compd. 490 (2010) 282.
[41] Y. Osumi, Suiso-kyuzo-goukin no Syurui to Sono, new edition, Agune Technology Center, Tokyo, Japan, 1999, p. 218.
[42] T. Gao, X. Qi, B. Chen, Chin. J. Nonferr. Met. 15 (2005) 1092.
[43] S. Wakao, Y. Yonemura, J. Less-Comm. Met. 89 (1983) 481.
[44] L.B. Wang, H.T. Yuan, Y.J. Wang, H.B. Yang, Q.D. Li, Y.N. Lin, Y.S. Zhang, J. Alloys Compd. 319 (2001) 242.
[45] L. Schlapbach, A. Züttle, Nature 414 (2001) 353.
[46] C. Iwakura, W.K. Choi, S. Zhang, H. Inoue, Electrochim. Acta 44 (1998) 1677.
[47] M. Au, F. Pourarian, S.G. Sankar, W.E. Wallace, L. Zhang, Mater. Sci. Eng. B 33 (1995) 53.
[48] F. Li, K. Young, T. Ouchi, M.A. Fetcenko, J. Alloys Compd. 471 (2009) 371.
[49] M. Pourbaix, Atlas of Electrochemical Equilibria in Aqueous Solution, 2nd English edition, NACE, Houston, TX, USA, 1974, p. 275.